Lab on a Chip

PAPER

Cite this: *Lab Chip*, 2025, **25**, 6650

Sequential trench well based microfluidic platform to isolate bacteria from whole blood with large volume processing

Cheonggyu Lee,†[a] Gi Yoon Lee,†[b] Hyerin Joo,[c] Hamin Kim,[c] Junwon Kang,[c] Tae Hyun Kim,[d] Jonghyun Ha,*[a] Sunghoon Kwon *[bc] and Jungil Choi *[a]

Received 30th September 2025,
Accepted 27th October 2025

DOI: 10.1039/d5lc00931f

rsc.li/loc

The separation of bacteria from infected blood is a crucial step for downstream bacterial detection and analysis. However, the extremely low bacterial concentration and high proportion of blood cells present significant challenges for effective separation. In this study, we present a microfluidic-based approach utilizing a sequential trench well structure that leverages the sedimentation-based separation process to effectively isolate bacteria from whole blood. Experimental results demonstrated that the system achieved an RBC removal rate of over 99.99%, while maintaining a bacterial recovery rate of up to nearly 78%. We utilized the separation platform to isolate bacteria from whole blood samples and applied separated bacterial samples to the image-based antimicrobial susceptibility testing (AST) process, reducing the conventional AST procedure by up to 42.18 hours. Our separation technology provides a simple and effective method for isolating bacteria from blood samples, with potential applications in infection diagnostics and microbiological analysis.

Introduction

Bacteremia, the presence of bacteria in the bloodstream, can lead to bloodstream infection (BSI) and progress to sepsis, which poses life-threatening risks. Sepsis, a dysregulated response to infection, occurs in more than 40 million cases and has a 20–50% mortality rate.[1,2] Additionally, delays in initiating effective treatment have been shown to significantly impact patient outcomes, with decreasing survival rate by approximately 7.6% per hour when appropriate antimicrobial therapy is not administered in a timely manner.[3] Therefore, the timely administration of optimal antimicrobial therapy is crucial.

To achieve rapid and optimal treatment, separation of bacteria from blood is essential, enabling downstream identification of pathogens and antimicrobial susceptibility testing (AST).[4–6] However, the initial bacterial concentration in blood is extremely low, typically ranging from 1–100 CFU mL^{-1}, whereas red blood cells are present at concentrations exceeding 10^9 cells per mL,[7,8] posing a significant challenge for bacterial isolation. Current diagnostic workflows rely on blood culture, followed by pure culture isolation using selective media to obtain bacteria free from blood components. While effective, this sequential process requires at least two days for bacterial enrichment and separation, delaying subsequent diagnostic steps such as pathogen identification and AST. These prolonged turnaround times highlight the need for alternative, rapid bacterial separation strategies to accelerate diagnostic workflows and enable timely antimicrobial intervention.

To enable faster bacterial separation, various physical separation techniques have been explored, including filtration,[9,10] centrifugation,[11–13] inertial[14–16] and elasto-inertial[17] separation, dielectrophoresis (DEP),[18] acoustophoresis[19,20] and magnetic-based separation.[21,22] However, these methods have several limitations. Clogging may occur due to RBC accumulation on the filter surface, which restricts bacterial movement (filtration). Separation efficiency is often low (centrifugation-based separation, inertial microfluidics), and a high bacterial concentration is required for effective separation (inertial, DEP, acoustophoresis). In addition, processing is limited (DEP, elasto-inertial microfluidics), and selectivity is restricted to specific bacterial strains (magnetic beads). These techniques also rely on external components such as electrodes, piezoelectric transducers, pumps, or centrifuges, which increase system complexity and operational cost.

[a] *Mechanical Engineering, Ajou University, 206, World cup-ro, Yeongtong-gu, Suwon-si, Gyeonggi-do, Republic of Korea. E-mail: hajh@ajou.ac.kr, cji@ajou.ac.kr*
[b] *Electrical and Computer Engineering, Seoul National University, Gwanak-gu, Seoul, Korea. E-mail: skwon@snu.ac.kr*
[c] *Interdisciplinary Program in Bioengineering, Electrical and Computer Engineering, Seoul National University, Gwanak-gu, Seoul, Korea*
[d] *KU-KIST Graduate School of Converging Science and Technology, Korea University, Seongbuk-gu, Seoul, Korea*
† These authors contritubed equally.

Gravity-based separation has emerged as a promising alternative to overcome these limitations. By exploiting differences in sedimentation velocity, this approach enables the separation of various types of cells without imposing strong shear stress or pressure, thereby preserving cell viability.[23–25] In addition, this method allows for the high-purity isolation of the desired target fraction and offers a simplified experimental workflow without requiring external or complex components.[26–28] However, previous gravity-based methods generally suffer from large volume processing with low throughput, making them unsuitable for the separation of bacteria from blood samples.

To address these issues, gravity-driven sedimentation has been integrated with microfluidic components to enable more efficient bacterial separation. Microfluidic chips allow for precise fluid control within microchannels[29,30] and enable sequential processing with increased throughput, facilitating the rapid and efficient separation of large blood sample volumes.[31,32] Additionally, they allow for direct sample collection after the experiment, making post-experimental observation more convenient.[33–35] These features help overcome the limitations of traditional gravity-based approaches.

By integrating these advantages, this study presents a structured microfluidic chip that leverages differential sedimentation velocities of blood cells and bacteria for effective bacterial separation (Fig. 1a). This platform implements simultaneous bacterial cultivation and separation process of bacteria from blood cells, preserving bacterial viability while minimizing bacterial loss. It enabled large-volume processing of blood samples, which addresses limitations of previous sedimentation-based microfluidic separation techniques. When applied to bacteria-spiked blood samples, the separation chip achieved nearly 10 000-fold reduction of blood cells and up to nearly 78% efficiency in bacterial recovery. Following minimal incubation, purified samples isolated by separation chip from whole blood samples were integrated with microscopic imaging-based rapid antimicrobial susceptibility testing[22,36] and showed a reduction in total lead time of up to 42.18 hours compared with conventional AST process, which demonstrates potential applicability to rapid BSI diagnosis.

Results and discussion

Chip design and operation

To enhance the efficiency of blood cell and bacteria separation based on gravity-driven sedimentation velocity

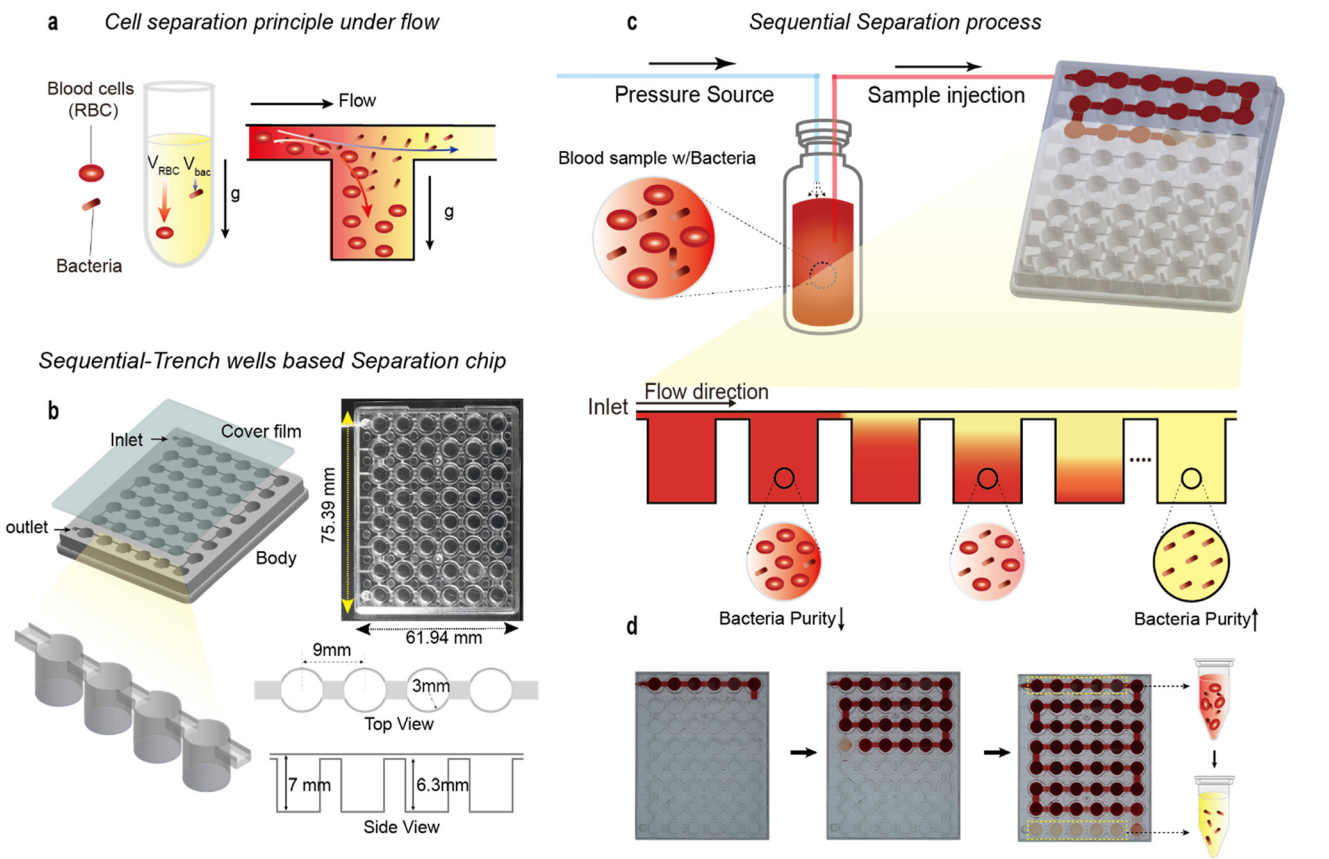

Fig. 1 Design and separation process of sequential trench well based microfluidic chip. (a) Schematic of separation principle based on difference of sedimentation velocity between blood cells and bacteria. (b) Design and dimension of separation chip. (c) Schematic of blood sample separation in the designed chip. (d) Captured images of separation process during flow operation.

differences and for processing large sample volumes, we designed a microfluidic chip incorporating a sequential trench well structure (Fig. 1b). The chip body consists of 48 wells, each with a radius of 3 mm and a height of 7 mm, which are interconnected at the top by microfluidic channels with a height of 0.7 mm. This channel height was chosen to regulate shear stress within an optimal range for maintaining RBC aggregation and sedimentation, consistent with previous reports showing that shear rates above ~50 s^{-1} disrupt RBC aggregation.[37] After fabrication, the chip was sealed with a PET film to ensure stable flow without leakage. To allow air to escape during sample loading, a small hole was created at the final well (marked as the outlet in Fig. 1b), which served as an air vent while the sample sequentially filled the wells. The sample came into contact with the adhesive part of the cover film, and we confirmed that the adhesive components did not affect bacterial viability and were biocompatible (Fig. S1). Each well can hold more than 197 μL, enabling the processing of a total sample volume of 9.5 mL. When the blood sample is introduced into the chip, it sequentially fills and flows through the wells using a pressure-driven flow setup (Fig. S2). Due to the rapid sedimentation velocity of red blood cells (RBCs), they quickly accumulate at the bottom of each well, while the supernatant containing bacteria flows into the next well (Fig. 1c). This stepwise operation results in a gradual depletion of RBCs as the fluid progresses through the chip, leading to an increasingly purified bacterial suspension in the final row of wells (Fig. 1c and d).

Mechanical analysis of sedimentation velocity

To understand the gravity-driven separation of RBCs, we analyzed the sedimentation velocity of suspended particles in a fluid, both theoretically and experimentally. A particle immersed in a fluid experiences three primary forces: a downward gravitational force, F_g, due to its own weight, an upward buoyant force, F_b, arising from fluid displacement, and a viscous drag force, F_d, opposing its motion. As these forces reach equilibrium, the particle attains a constant velocity known as the sedimentation velocity. This principle governs the separation of particles in fluids and is particularly relevant to the microfluidic sorting of biological components, including RBCs. This sedimentation velocity can be mathematically described using Stokes' flow theory,[38] which applies to small spherical particles moving in a viscous fluid under low Reynolds number conditions. The forces acting on a settling particle include the downward gravitational force $F_g \sim R^3\rho_p\, g$, the buoyant force $F_b \sim R^3\rho_l\, g$, and the opposing viscous drag force $F_d \sim \mu R u_s$, where R is the particle radius, ρ_p and ρ_l are the densities of the particle and liquid, respectively, g is the gravitational acceleration, μ is the viscosity of the fluid, and u_s is the sedimentation velocity. By balancing the forces, $F_g \sim F_b + F_d$ (Fig. 2a), we obtain the sedimentation velocity, $u_s \sim (\rho_p - \rho_l)gR^2/\mu$. This expression shows that sedimentation velocity increases with the size and density difference of the particle while decreasing with increasing fluid viscosity.

Considering the trench volume, V, and the cross-sectional area, A, the settling time can be theoretically expressed as $\tau \sim$

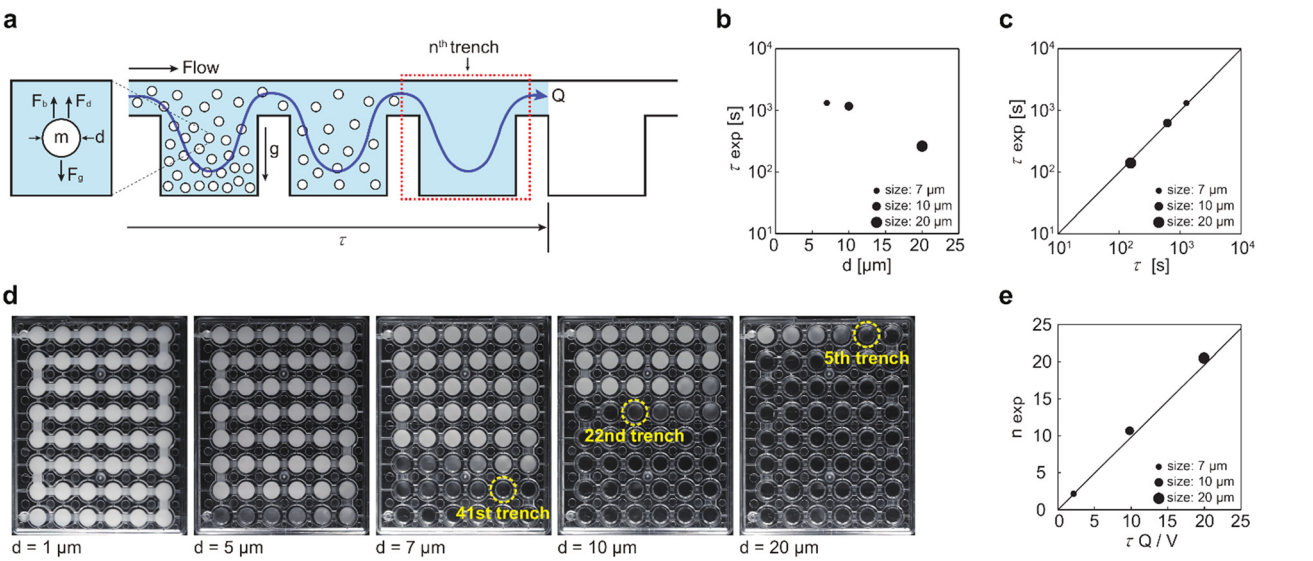

Fig. 2 Sedimentation of dense particles in a liquid. (a) Schematic of particle sedimentation in a microfluidic trench, including the definition of the settling time τ across n trenches. Inset: Free-body diagram of a spherical particle in the liquid. (b) Experimental measurements of settling time (τ_{exp}) for various particle sizes. (c) Comparison between experimentally measured settling time, τ_{exp}, and theoretically predicted settling time, τ. The plot follows the relation $\tau_{exp} \sim \alpha\tau$, where α is a prefactor (α = 0.53) used to precisely fit the experimental results. (d) Experimental visualization of polystyrene bead sedimentation (1 μm, 5 μm, 7 μm, 10 μm, and 20 μm) in the microfluidic chip, showing size-dependent settling behavior. (e) Comparison between experimentally determined trench number n and theoretical predictions based on $n \sim \tau Q/V$. Data points in (b), (c), and (e) represent mean values from three independent experiments. Error bars are present but may be obscured by the marker symbols.

$V/(u_s A)$. This formulation assumes that the particle settles over a vertical distance approximately equal to the trench depth, which is geometrically represented by the ratio V/A. Substituting the Stokes' law result for sedimentation velocity, $u_s \sim (\rho_p - \rho_l)gR^2/\mu$, into the time expression yields $\tau \sim \mu V/[(\rho_p - \rho_l)gR^2A]$. This relation provides an estimate of the timescale for particles to settle from the top to the bottom of the trench and represents the time required for an incoming particle to sediment and separate within a specific well (the nth trench). From this expression, it is evident that the settling time increases with higher μ, as greater resistance from the fluid slows down particle motion. Conversely, a larger density difference, $\rho_p - \rho_l$ between the particle and the fluid reduces the settling time, as the gravitational driving force becomes stronger. Additionally, larger particle R leads to shorter settling times, since larger particles experience a greater gravitational force relative to drag.

To determine where particle-fluid separation occurs within the microfluidic chip, we relate the previously defined settling time τ to the transport timescale of the flow (Fig. 2a). In a microfluidic device with a volumetric flow rate Q, the fluid residence time per trench can be approximated as V/Q, indicating how long the fluid and suspended particles stay within each trench before being transported to the next trench. If each trench contributes a time increment of V/Q, then the total time available for sedimentation across n trenches is $n(V/Q)$. Equating this to the settling time yields the scaling law $n \sim \tau Q/V$. This relation allows prediction of the trench index at which effective separation occurs. By adjusting flow rate Q, trench geometry (*e.g.*, V and A), particle properties (*e.g.*, R and ρ_p), and fluid properties (*e.g.*, μ and ρ_l) the system can be tuned to control the location of particle–fluid separation within the chip.

Parametric study on particles and fluid properties

To experimentally validate the theoretical modeling of t and n, a parametric study was conducted to investigate the influence of particle size on sedimentation velocity. While red blood cells (RBCs) and bacteria have similar densities (RBC: 1.086–1.122 g cm^{-3}, *E. coli*: 1.08–1.10 g cm^{-3}),[12] RBCs have a larger diameter than bacteria. Based on this, it was hypothesized that RBCs and bacteria would separate primarily due to their size differences. To validate this principle, polystyrene microbeads with identical densities but varying diameters (1 μm, 5 μm, 7 μm, 10 μm, and 20 μm) were introduced into the separation chip. Among these, 1 μm beads were selected to approximate the size of bacteria, while 7 μm beads were chosen to mimic RBCs, enabling a direct comparison of their relative sedimentation velocities.

The separation behavior in the chip exhibited a strong dependence on particle size (Fig. 2d). Separation and sedimentation were defined as the point at which the turbidity (pixel intensity) of well decreased below 30% relative to the first well (Fig. S3). The 1 μm and 5 μm beads showed no significant sedimentation and were distributed throughout the chip, whereas beads larger than 7 μm sedimented and separated in earlier wells (representative separation positions for 7, 10, and 20 μm beads: 41st, 22nd, and 5th trenches, respectively). Based on this criterion, the measured sedimentation times for 7, 10, and 20 μm beads were 2486 s, 1172 s, and 263 s, respectively (Fig. 2b). These values were compared with theoretical predictions based on the equation $\tau \sim \mu V/[(\rho_p - \rho_l)gR^2A]$. To enable direct comparison, the theoretical values were normalized by introducing a constant prefactor α, such that $\tau_{exp} \sim \alpha\tau$. The prefactor α accounts for physical factors and geometric details that are neglected in the idealized theoretical model. Specifically, the derivation of the theoretical expression assumes perfect spherical particles, uniform initial vertical position within the trench, negligible wall effects, and instantaneous response to gravitational acceleration. In practical microfluidic systems, however, deviations such as particle dispersion, finite entrance time, and lateral motion can result in longer effective settling times. Additionally, small differences in particle–fluid interaction near boundaries or between wells may introduce systematic offsets that the scaling law does not capture. Thus, the prefactor serves as an empirical correction that aligns the theoretical scaling with observed dynamics while preserving the underlying physical dependencies. In our study, the fitted prefactor was found to be approximately 0.53, which is consistent with previously reported values for similar systems and falls within a reasonable range considering the approximations involved.[39] The comparison revealed a strong linear correlation between the experimentally measured and theoretically predicted sedimentation times, supporting the validity of the scaling model across a range of particle sizes (Fig. 2c). Furthermore, the number of trenches required for separation, n, also showed a linear relationship with the theoretical scaling $n \sim \tau Q/V$ (Fig. 2e). These results suggest that smaller particles such as bacteria remain suspended and migrate to later wells, whereas larger particles such as RBCs settle earlier and separate near the front of the chip, thereby enabling effective separation.

To further investigate the effects of particle density and solution viscosity on particle separation and sedimentation time, we conducted comparative experiments. The sedimentation time of three different 3 μm diameter bead suspensions with distinct densities—polystyrene (1.05 g cm^{-3}), polymethacrylate (1.19 g cm^{-3}), and melamine resin (1.51 g cm^{-3})—was measured to assess the extent of density-based separation. The experimental results indicated that the measured sedimentation times deviated from theoretical predictions, with values ranging from 2124 s for 1.19 g cm^{-3} to 1476 s for 1.51 g cm^{-3}, indicating a clear trend in which higher-density particles settled more rapidly. The corresponding n values were 29 and 22 for polymethacrylate (1.19 g cm^{-3}) and melamine resin beads (1.51 g cm^{-3}), respectively, further confirming that higher-density particles separate earlier in the chip (Fig. S4).

Additionally, solutions with different viscosities containing 10 μm diameter melamine resin (1.51 g cm^{-3}) were prepared by adjusting the glycerol ratio in deionized water (DW), and the degree of sedimentation was analyzed. As viscosity increased, a corresponding increase in sedimentation time (*i.e.*, a decrease in sedimentation velocity) was observed. The measured sedimentation times were 380 s for 1.76 cP, 296 s for 1.31 cP, and 188 s for 1.005 cP, highlighting the effect of fluid viscosity on the sedimentation process. The associated n values were 7, 6, and 4, respectively, demonstrating that higher viscosity delays particle separation to later trenches in the chip (Fig. S5).

Although the experimentally measured sedimentation times did not perfectly match theoretical predictions, a strong linear correlation was observed in the trends for particle size, density, and viscosity, supporting the theoretical model. The discrepancies between theoretical and experimental values are likely due to the fact that Stokes' Law assumes sedimentation in a quiescent (non-flowing) fluid, whereas the experiment was conducted in a flowing system with microfluidic structures. The fluid flow and geometric constraints of the microfluidic chip introduce additional factors that may alter sedimentation behavior compared to the theoretical expectation.

Effect of blood viscosity and flow rate on sedimentation-based separation

In addition to the parametric analysis with particle size, density, and fluid viscosity, further experiments were conducted using blood–culture medium mixed samples to evaluate how sample viscosity and flow rate influence sedimentation-based separation in the trench wells. Viscosity measurements showed that whole blood had a viscosity of ~13.6 mPa s at the shear rate corresponding to the chip (≈8.5 s^{-1}), creating unfavorable conditions for sedimentation (Fig. S6).

To address this, separation experiments were performed with diluted samples at blood : culture medium ratios of 1 : 1, 1 : 2, and 1 : 3. As the dilution increased, the viscosity decreased and the effective separation position shifted forward, with RBCs observed up to approximately the 41st, 39th, and 38th wells, respectively (Fig. S7). Under the 1 : 3 dilution condition, the viscosity of the sample was measured to be ~2.5 mPa s at the chip shear rate (≈8.5 s^{-1}) (Fig. S6), and because viscosity generally decreases with increasing temperature,[40] the effective viscosity during experiments at 37 °C would be slightly lower.

Since this dilution ratio is also routinely used in clinical practice, we adopted the same ratio in our experiments. Subsequently, additional separation experiments were carried out at three flow rates (118, 136, and 180 μL min^{-1}). The results demonstrated that as the flow rate increased, sedimentation was progressively delayed, with RBCs filling up to approximately the 38th, 40th, and 41st wells, respectively, before being effectively depleted (Fig. S8). These observations are consistent with previous reports that flow rate is a critical factor influencing sedimentation behavior by altering residence time and shear conditions in confined channels.[41–43] Therefore, subsequent experiments were performed at about 100 μL min^{-1}, which provided a balance between sufficient sedimentation efficiency and the sample volume required for downstream analysis.

Removal performance of blood cells in separation chip

After setting the flow rate conditions for particle separation based on parameter analysis, the performance for depleting blood cells in the separation chip was evaluated. Blood samples diluted 1 : 3 in medium (total 9.5 mL) were introduced into the separation chip, with the flow directed to sequentially fill the wells from A1 to H1 (Fig. 3a). After the sample reached the final H1 well, aliquots were collected from one well in each row along the flow direction, and from four wells in the last H row (A1, B6, C1, D6, E1, F6, G1, H6, H4, H2, and H1). The blood cell concentration in each collected sample was quantified using a hemacytometer.

Following the separation process, inspection of the chip images revealed that most of RBC sedimentation into the trench wells was observed in the front region (rows A to E), and, as a result of this upstream depletion, rows F to H displayed lighter regions (Fig. 3b and c). Measurement of the extracted samples revealed that the initial RBC concentration (7.98×10^9 mL^{-1}) decreased to approximately 6.65×10^8–3.77×10^9 mL^{-1} in the front region (rows A–E), where RBC sedimentation occurred. In contrast, a significant reduction to the order of 10^5 mL^{-1} (1–5×10^5 mL^{-1}) was observed in the separated region (rows G–H, lighter regions) (Fig. 3b and c). Based on these results, the RBC depletion rate (%) was calculated, showing a progressive increase along the wells and reaching a maximum efficiency of 99.993–99.998% in the final H row.

In addition, the separation efficiency of leukocytes (white blood cells - WBC) along the flow direction was evaluated (Fig. S9). Starting from the initial concentration (3.09×10^6 mL^{-1}), leukocytes rapidly sedimented in the front rows, resulting in increased concentrations in those wells. In contrast, no cells were detectable in the final H row by image inspection, corresponding to concentrations below 10^4 mL^{-1}. Based on concentration measurements, the depletion efficiency was calculated, showing a maximum of 99.676% in the H row.

This distribution of concentration of RBCs aligns with the sedimentation mechanism within the separation chip. As the sample flows through the chip, RBCs settle due to gravitational and sedimentation forces, leading to their gradual removal in the early wells (Fig. 3b and c, A–E rows). Consequently, as the fluid continues to flow downstream, the RBC concentration in the upper fluid layer decreases, resulting in a significant reduction in later wells (Fig. 3b and c, F–H rows).

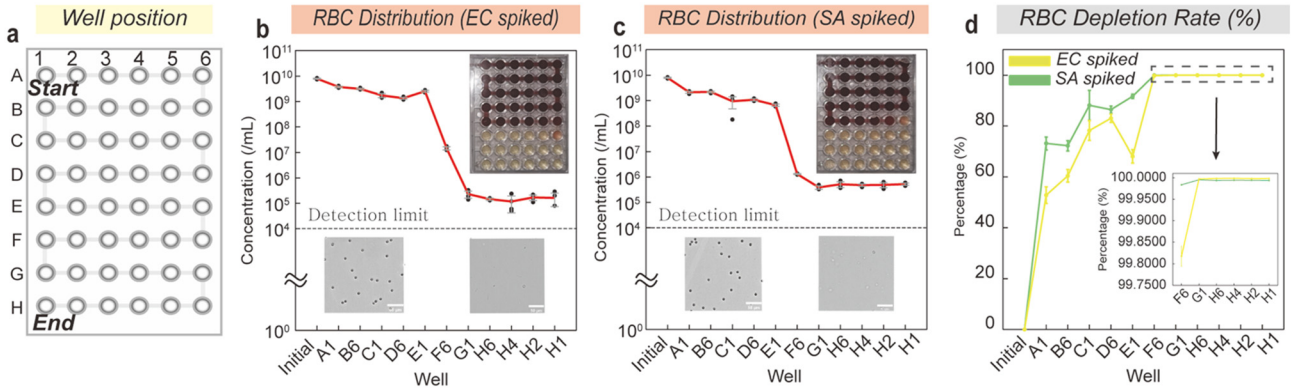

Fig. 3 Separation of red blood cells and depletion performance. (a) Well position of separation chip. (b) Distribution of residual RBC concentrations in each trench well along the flow direction using *E. coli*-spiked samples. (c) Distribution of residual RBC concentrations in each trench well along the flow direction using *S. aureus*-spiked samples. (d) Change in RBC depletion rate according to well positions for *E. coli*-spiked and *S. aureus*-spiked blood samples.

Additionally, the structural characteristics of the microfluidic chip prevent already-settled RBCs from re-entering the suspension as the upper fluid moves forward. As a result, the later wells primarily contain the upper fluid, which is relatively depleted of RBCs. This process consistently explains the observed sedimentation and concentration gradients, demonstrating that the microfluidic chip effectively separates blood cells based on sedimentation principle.

Bacterial detection and recovery performance of separation chip

We evaluated not only the efficiency of blood cell removal but also the bacterial detection and separation performance of the chip. To this end, diluted blood samples were spiked with bacteria at concentrations ranging from 10^1 to 10^4 CFU mL^{-1}, processed through the chip, and the recovered bacterial concentrations were quantified. Since downstream analyses rely on fractions in which blood cells are maximally removed, the supernatant collected from the H row was spread on agar plates to determine bacterial recovery and concentration.

For *E. coli*, colonies were detected at input concentrations as low as 10^2 CFU mL^{-1} (Fig. 4a and c), and the recovered concentrations remained within the same order of magnitude as the input across all tested conditions (Fig. 4a). In contrast, *S. aureus* was consistently detected only from 10^3 CFU mL^{-1} (Fig. 4b and c), and the recovered concentrations were approximately one order of magnitude lower than the corresponding input concentrations (Fig. 4b).

To investigate species-dependent differences in separation efficiency, we further examined bacterial concentration profiles across wells along the flow direction using samples spiked at 10^4 CFU mL^{-1}. For *E. coli*, the concentration gradually decreased from 9.9×10^4 CFU mL^{-1} in well A1 to 3.1×10^4 CFU mL^{-1} in well H6, but remained above 10^4 CFU mL^{-1} overall (Fig. 4d).

In contrast, *S. aureus* exhibited a pronounced decrease, from 4.8×10^4 CFU mL^{-1} in well A1 to 3.1×10^3 CFU mL^{-1} in well H1, representing more than a one-order reduction (Fig. 4e). These results indicate that while *E. coli* remains suspended during flow and can be recovered efficiently downstream, *S. aureus* tends to sediment more rapidly, leading to reduced recovery in downstream wells, a higher detection limit, and lower overall separation efficiency.

Taking into account bacterial doubling during the separation process, recovery efficiencies in the H row were calculated relative to a growth control (G.C.), a bacteria spiked blood sample incubated separately during the separation period. Under these conditions, the recovery rate was 77.66% for *E. coli* and 13.10% for *S. aureus* (Fig. 4g).

We hypothesized that the increased sedimentation rate and the resulting low recovery efficiency of *S. aureus* could be attributable to its interactions with blood components.[44] Previous studies have shown that *S. aureus* secretes extracellular staphylo-coagulase, which interacts with plasma prothrombin to form staphylo-thrombin aggregates.[45] In addition, *S. aureus* has been reported to interact with RBCs in the presence of plasma proteins such as fibrinogen and IgG.[46] These interactions may promote the formation of larger aggregates containing *S. aureus*, thereby increasing sedimentation velocity and reducing bacterial recovery in our separation method.

To test this hypothesis, we performed separation experiments under identical conditions using pure bacterial suspensions prepared in culture medium without blood components. Under these conditions, the bacterial concentration was maintained at a relatively uniform level across the wells. *E. coli* achieved a recovery rate of 85.19% and *S. aureus* reached 73.93%, substantially higher than in the presence of blood (Fig. S10). These findings support the hypothesis that the reduced separation efficiency of *S. aureus* could be attributed to its interactions with blood components. Collectively, the results suggest that, in blood, the separation process can be affected not only by physical

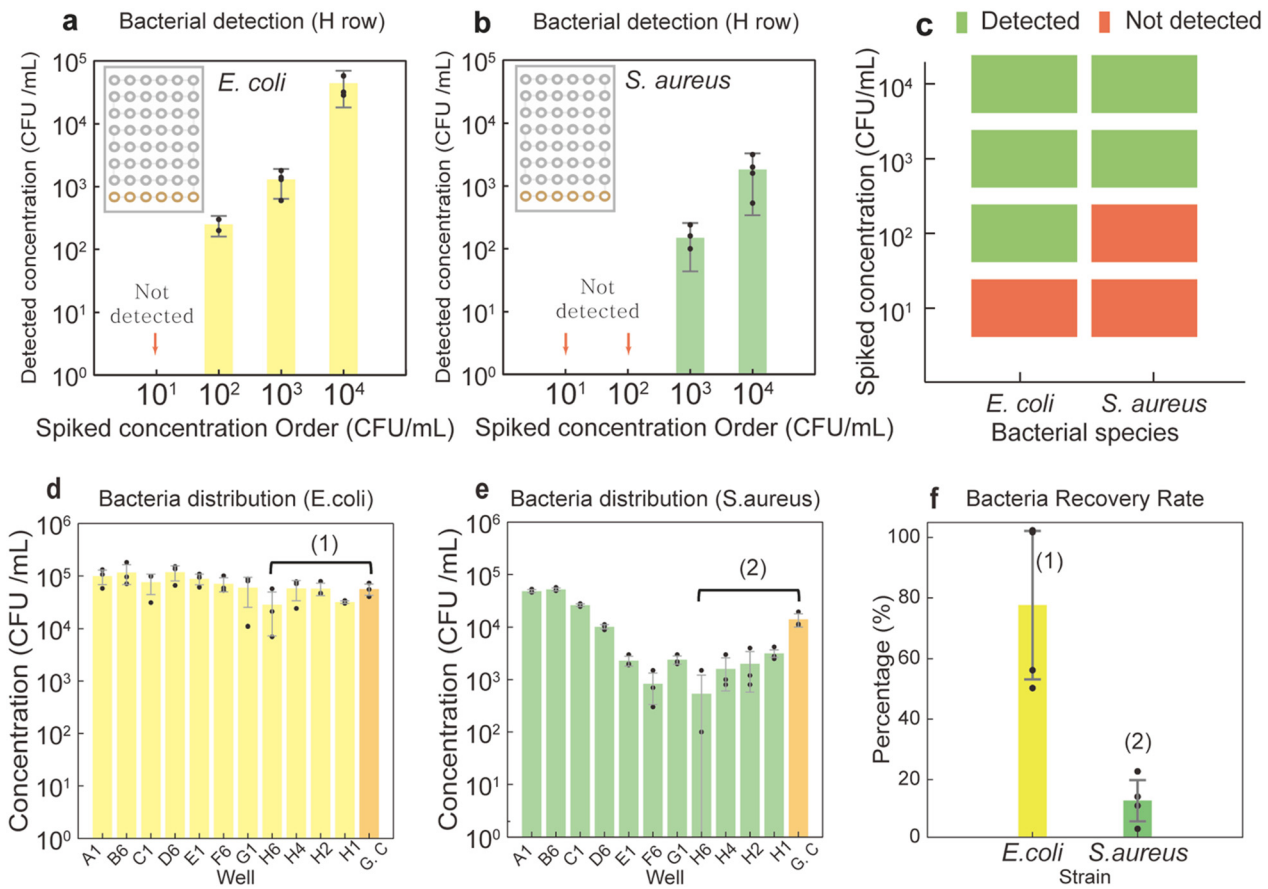

Fig. 4 Performance of separation of bacteria in sequential trench wells. (a) Detected concentration of *E. coli* according to spiked bacterial concentration. (b) Detected concentration of *S. aureus* according to spiked bacterial concentration. (c) Detection outcome according to spiked bacterial concentration. (d) Distribution of bacteria concentration along the wells using *E. coli*-spiked blood sample of 10^4 CFU mL^{-1}. (e) Distribution of bacteria concentration along the wells using *S. aureus*-spiked blood sample of 10^4 CFU mL^{-1}. (f) Recovery rate of bacteria in separation process. The recovery rate was calculated by normalizing the concentration in row H to that of the growth control (G.C).

properties (size variation) but also by interactions with biochemical components of the sample matrix.

Application of separation process to downstream analysis for rapid antimicrobial susceptibility testing (AST)

To demonstrate the applicability of the separation chip in bloodstream infection (BSI) diagnostics, we utilized the device to isolate bacteria from blood samples and subsequently applied the purified sample to an antimicrobial susceptibility test (AST).

To mimic the condition of bloodstream infection, bacteria were spiked into whole blood at a final concentration of 30 CFU mL^{-1}, followed by mixing with blood culture medium and a pre-culture step (Fig. 5a_i). After incubation, the separation chip was used to isolate bacteria from blood cells, and the bacterial fraction collected from the final row (row H) was subjected to AST (Fig. 5_ii). The purified sample was diluted in a 1% agarose matrix and loaded onto a customized AST chip that contained dried antimicrobials for time lapse imaging-based analysis (Fig. 5a_iii). Residual blood cells were visible in the initial time (0 h); however, their appearance did not change over time. In contrast, bacteria underwent division and colony enlargement, which enabled clear distinction between blood cells and bacterial colonies (Fig. S11).

For each antibiotic and time point, images were binarized to quantify bacterial growth as colony area. To determine the minimum inhibitory concentration (MIC), drug-free control wells were analyzed, and the time point at which the colony area exceeded a predefined threshold (binary value 10 000) was defined as growth positive. Growth in antibiotic-treated wells was then normalized to the control growth at 2 hours after this point (Fig. S12a). Bacterial inhibition was defined as a normalized growth value below 0.2, and the lowest antibiotic concentration meeting this criterion was designated as the MIC. Using this approach, MIC values were determined within 4 hours for *E. coli* and within 6 hours for *S. aureus* (Fig. 5b–d and S12b–d).

To evaluate the performance of the system across multiple antibiotics, AST was performed for 9 antibiotics against *E. coli* and 7 antibiotics against *S. aureus*. MIC values of all 16 antibiotics by rapid AST process fell within the target QC range and all MIC values were within one

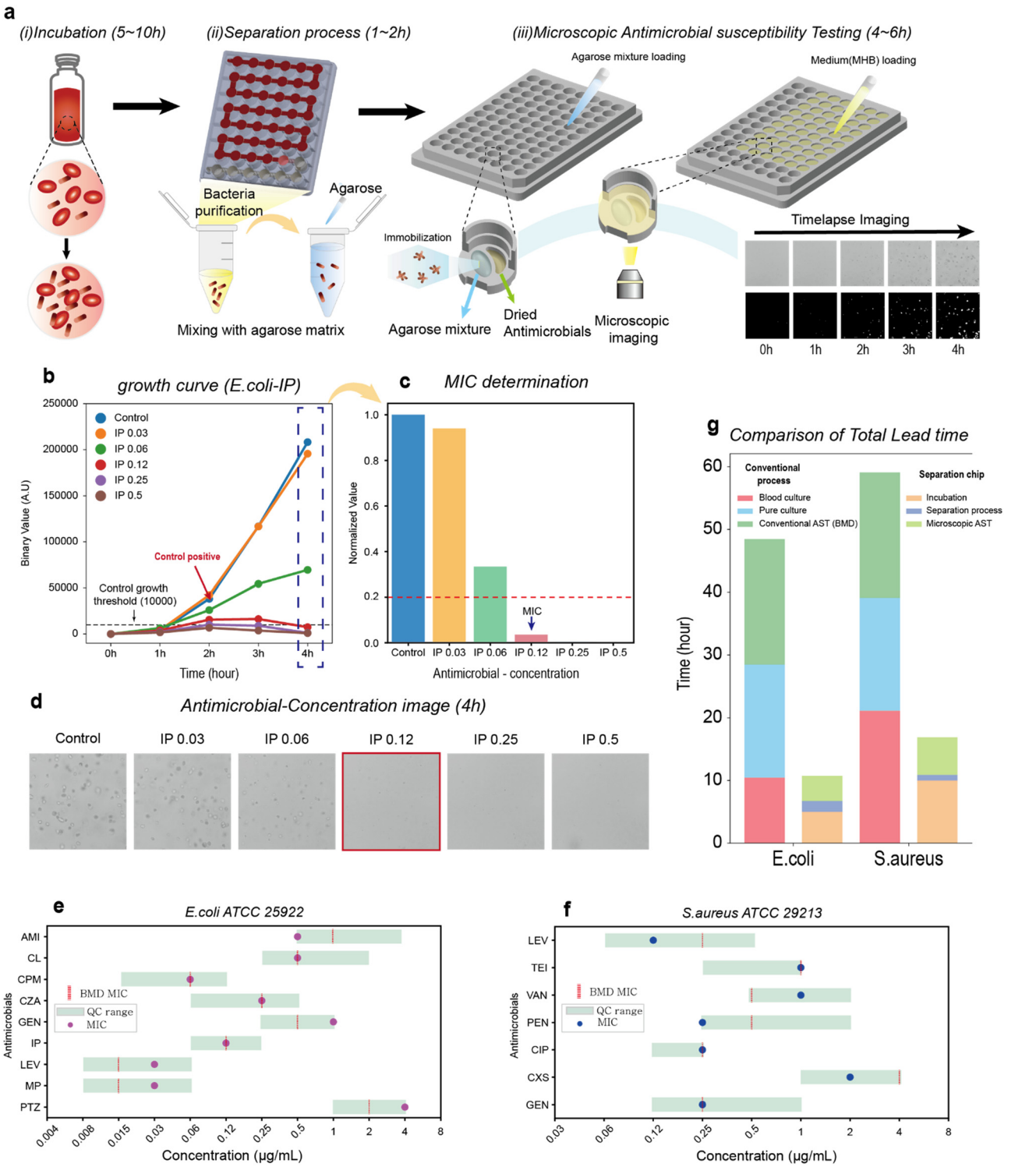

Fig. 5 Demonstration and results of rapid AST process using separation chip from whole blood samples. (a) Experimental steps for imaging based rapid AST using the separation chip. (b) Growth curve (binary value of images) of imipenem(IP)-treated *E. coli* in a rapid AST process. (c) Normalized value of growth curve in 4 hours and MIC determination. (d) Representative images of various concentrations of imipenem (IP) in 4 hours. (e and f) MIC results of *E. coli* (ATCC 25922) and *S. aureus* (ATCC 29213) by rapid AST process and comparison with MIC of broth microdilution (BMD) within target range (QC range). (g) Comparison of Total Lead time between conventional method and proposed method.

2-fold range (100% of essential agreements) compared with that of reference (BMD) (Fig. 5e and f), confirming compatibility and accuracy of proposed AST workflow.

Moreover, the separation process significantly shortened the overall diagnostic timeline. While conventional blood culture and pure culture methods required 28.45 hours for *E.*

coli and 39.08 hours for *S. aureus*, the proposed separation process reduced these times to 6.72 hours and 10.9 hours, respectively. Additionally, the entire AST process was completed within 10.72 hours for *E. coli* and 16.9 hours for *S. aureus*, reducing the total lead time by 37.73 and 42.18 hours, respectively, compared to the conventional AST process (Fig. 5g). These results highlight the potential of the separation chip as a rapid and reliable tool for bloodstream infection diagnostics and AST.

Conclusion

In this study, we developed a microfluidic chip for bacterial isolation from whole blood, optimized through the integration of chip design, fluid dynamics, and differences in sedimentation velocity. The system achieved efficient separation, with a high red blood cell (RBC) removal rate of 99.993–99.998%, while maintaining bacterial recovery rates of 77.66% for *E. coli* and 13.10% for *S. aureus*. Moreover, the bacteria separated by the proposed microfluidic chip were successfully applied to rapid antimicrobial susceptibility testing (AST), reducing the overall diagnostic time by up to 42.18 hours compared with conventional methods.

Compared with other separation methods (Table S1), our approach achieved one of the highest blood cell removal efficiencies (up to 99.998%) while maintaining high bacterial recovery in the case of *E. coli*. When both bacterial recovery and RBC removal were considered together, the separation efficiency—defined as previously reported in[11]—reached 38 800, which is among the highest values reported (Fig. S13a and b). These results indicate that our method has a distinct advantage in removing interfering blood components, thereby facilitating downstream analyses such as antimicrobial susceptibility testing (AST) and pathogen identification.

However, despite the ability to process relatively large sample volumes (9.5 mL), the total processing time of 90 min remains a limitation, resulting in relatively low total throughput compared with other techniques (Fig. S13c and d). In contrast, when performance was normalized to the equivalent processing of 1 mL of whole blood—accounting for the different dilution ratios across methods—our approach enabled faster processing than methods requiring higher dilution, thereby demonstrating higher throughput for processing actual whole blood (Fig. S13e).

The proposed system provides an efficient approach for bacterial separation from blood samples, with potential applications in bloodstream infection diagnosis, infectious disease research, and microbiological analysis. However, the current system requires AST to be performed separately, and it does not fully reproduce the biological complexities of actual clinical samples, such as plasma protein variability, platelet aggregation, or bacterial sequestration by phagocytes. To address this limitation, we will implement whole process using actual clinical samples for real-world applications. Moreover, we will focus on developing a fully integrated microfluidic platform capable of simultaneously performing bacterial identification (ID) and AST, enabling a streamlined and comprehensive diagnostic process. This advancement would facilitate the transition from laboratory-based tests.

Material and methods

Separation chip design and fabrication

The separation chip was designed by 3D CAD software (Solidworks v2018, Dassault Systèmes SolidWorks Corp). Fabrication was implemented by injection molding with general purpose polystyrene (LG Chem). Fabricated microfluidic chips were treated with O_2 plasma and subsequently sealed using a 0.15 mm-thick transparent PET film (IZsolution, Korea). Sealed chips were sterilized by a 10 kGy electron beam irradiation (Greenpia Technology, Korea) and stored at room temperature.

Preparation of microbead solution

Polystyrene microbeads with diameters of 1 μm (CAT. 89904), 5 μm (CAT. 79633), 10 μm (CAT. 72986), 20 μm (CAT. 74491), and 30 μm (CAT. 84135), as well as beads with different densities—polystyrene (3 μm, 1.05 g cm^{-3}, CAT. 42922), polymethacrylate (3 μm, 1.19 g cm^{-3}, 86 935), and melamine resin (3 μm, 1.51 g cm^{-3}, CAT. 72439)—were all purchased from Sigma-Aldrich. All bead solutions were prepared by diluting the microbeads in deionized water (DIW) to a final concentration of 5% (v/v) in a total volume of 10 mL. Solutions with different viscosities were prepared by diluting glycerol (CAT. G5516, Sigma-Aldrich) in DIW at ratios of 9 : 1 (1.31 cP) and 4 : 1 (1.76 cP). Each viscosity-adjusted solution contained 10 μm melamine resin beads (1.51 g cm^{-3}, CAT. 94050, Sigma-Aldrich) at a concentration of 5% (v/v).

Sedimentation time analysis

The sedimentation time (t) was defined as the time required for a particle to sediment sufficiently within a given well such that a distinct separation was observed compared to the preceding well. To quantitatively assess sedimentation behavior in the microfluidic wells, both visual observation and image-based intensity analysis were performed. All experiments were recorded on video, and the determination of well separation was made by reviewing the recorded footage. First, the moment when a well was visually observed to be separated was identified, and the corresponding video frame was extracted for image analysis. The extracted frame was then imported into photoshop, where the intensity histograms of the first well and the well identified as separated were generated. Finally, if the average intensity of the identified well was reduced to less than 30% of the initial well's intensity, the well was considered to be separated.

Preparation of bacteria samples

Standard strains (*E. coli* ATCC 25922 and *S. aureus* ATCC 29213) were obtained from Microbiologics, Inc. (MN, United States). Bacterial stocks were prepared using 10% skim milk and stored at −80 °C. For experiments, thawed stock solutions were spread onto tryptic soy agar (TSA) plates (AsanPharm, Korea) and kept at 35 °C overnight. The resulting plates (F1 plates) were then stored at 4 °C. Before testing, bacterial colonies from F1 plates were inoculated and incubated into tryptic soy broth (TSB, BD Difco). Resulting culture suspension was adjusted to a turbidity equivalent to 0.5 McFarland standard (approximately 1–2 × 10^8 CFU mL^{-1}) using a nephelometer (Densichek Plus Standards, BIOMÉRIEUX). The measured suspensions were subsequently serially diluted in Mueller-Hinton broth (MHB; BBL™, BD, USA) to achieve the desired bacterial concentration prior to spiking into whole blood.

Blood collection and preparation

Blood samples were collected from healthy donors into EDTA tubes (BD vacutainer K2E, 367525). All experiments were performed in accordance with the guidelines of institutional review board of Ajou University (202411-HS-004), and experiments were approved by the ethics committee at Ajou University. Informed consents were obtained from human participants of this study. To create conditions similar to conventional blood culture, 3 mL of blood was mixed with 9 mL of blood culture medium (BacT/Alert culture media bottle 410851, bioMérieux, France). Subsequently, 1 mL of bacterial suspension was added to achieve the target bacterial concentration.

Flow experiment setup and condition

Flow was controlled using a pressure-based flow regulation system (CAT. LU-FEZ, Fluigent, France). Before the separation test, all samples (bead solutions, blood samples) were contained in glass vias (CAT. SL.Vi1331, DAIHAN Scientific, Korea) and sealed with a rubber-sealing cap (CAT. SL.Vi1286, DAIHAN Scientific, Korea). Sterilized magnetic stirrers were introduced in sample vials and continuously stirred during flow operation to prevent particle sedimentation within vials. Sealed vials were connected with two needles, one needle was connected to the pressure pump to introduce pressurized air, while the other needle was connected to microtubing (CAT. AAD04103, Saint-Gobain Performance Plastics, USA) attached to the separation chip, allowing the fluid to be introduced into the chip under controlled conditions. Parametric study using bead solution was conducted at room temperature, while separation experiments using blood samples and pure bacteria samples were implemented at 37 °C with incubation conditions (CAT. C-IND1, Changshin Science, Korea).

Rapid AST chip fabrication

96 well based Rapid AST chips that have chambers to load agarose matrix and antimicrobial agents in each well were designed by 3D CAD software (Solidworks v2018, Dassault Systèmes SolidWorks Corp). Fabrication was implemented by injection molding with general purpose polystyrene (LG Chem). All antimicrobial agents were purchased from Sigma-Aldrich except Avibactam from MedChemExpress. Antibiotics were stored as stock solutions at −80 °C and thawed prior to use. To prepare the desired test concentrations, the antibiotics were diluted in deionized water (DW). A 96-well microfluidic chip was treated with O_2 plasma to enhance surface wettability. The diluted antimicrobial solutions were then dispensed into the antimicrobial chambers of each well. The chips were dried at 50 °C under dry heat to immobilize the antimicrobial agents, followed by nitrogen packaging for storage at refrigerated conditions.

Red blood cell (RBC) counting

Blood cell–depleted samples collected from the chip were diluted in PBS, and 10 μL of each diluted sample was loaded onto a hemacytometer (Neubauer-Improved, MARIENFELD, Germany). The samples were imaged under a brightfield microscope (10× magnification), and the number of cells within the counting grids was manually enumerated to estimate the concentration.

Leukocyte (WBC) counting

For leukocyte counting, whole blood samples were mixed with ACK lysing buffer (Thermofisher Scientific, USA) at a 1 : 9 ratio and incubated at room temperature. The mixture was centrifuged at 500 × *g* for 5 min to obtain a WBC pellet. After discarding the supernatant, the pellet was washed once with 1 mL PBS by centrifugation to remove residual ACK. The pellet was then resuspended in 100 μL of Hoechst dye solution (Hoechst 33342, Life technologies, USA) prepared at 1 : 1000 dilution in PBS, and incubated for 30 min at room temperature in the dark. After incubation, 10 μL of the stained suspension was loaded onto a hemacytometer, imaged at 10× magnification, and analyzed by merging brightfield and fluorescence (DAPI channel) images. WBCs were manually counted within the counting grids.

Image based rapid AST process

The rapid antimicrobial susceptibility testing (AST) process was performed following the previously reported method.[22,36] The final row of samples, where blood cells had been separated in the separation chip, was mixed with 1.5 mL of 1% agarose solution and loaded into a 96-well rapid AST chip. After allowing the agarose to solidify for 10 minutes, 90 μL of Mueller-Hinton broth (MHB) was dispensed into each well. The AST chip was then placed in an automated microscopic imaging system (dRAST, QuantaMatrix) for timelapse imaging over 12 hours. Images are binarized and

processed by embedded software in an automated imaging system.

Conventional AST process

Blood culture was performed by inoculating 5 mL of blood into a blood culture bottle (product name, BD) along with 100 μL of bacterial suspension at the target concentration. Upon culture positivity, an aliquot of the blood culture sample was taken and streaked onto a tryptic soy agar (TSA) plate for pure culture, which was incubated for 20 hours. Following colony growth, broth microdilution (BMD) was conducted according to the previously reported method.[22,36]

Author contributions

C. Lee, G. Lee, J. Ha, S. Kwon and J. Choi led the development of the concepts, designed the experiments, and interpreted results. C. Lee and G. Lee led the experimental work with support from H. Joo, H. Kim, J. Kang. J. Ha performed the mechanical analysis. C. Lee, G. Lee, S. Kwon, J. Ha and J. Choi wrote the paper with support from T. Kim.

Conflicts of interest

There are no conflicts to declare.

Data availability

The data supporting this article have been included as part of the supplementary information (SI). Supplementary information is available. See DOI: https://doi.org/10.1039/d5lc00931f.

Acknowledgements

This study was supported by the Korea Disease Control and Prevention Agency (2024-ER2206-00) and supported by the Industrial Technology Innovation Program (RS-2024-00438958) funded By the Ministry of Trade, Industry & Energy (MOTIE, Korea) and the National Research Foundation of Korea (NRF) and the Commercialization Promotion Agency for R&D Outcomes (COMPA) grant funded by the Korea government (Ministry of Science and ICT) (RS-2024-00432752).

References

1 R. S. Hotchkiss, L. L. Moldawer, S. M. Opal, K. Reinhart, I. R. Turnbull and J. L. Vincent, *Nat. Rev. Dis. Primers*, 2016, **2**, 16045.
2 K. E. Rudd, S. C. Johnson, K. M. Agesa, K. A. Shackelford, D. Tsoi and D. R. Kievlan, *et al.*, *Lancet*, 2020, **395**, 200–211.
3 A. Kumar, D. Roberts, K. E. Wood, B. Light, J. E. Parrillo and S. Sharma, *et al.*, *Crit. Care Med.*, 2006, **34**, 1589–1596.
4 M. Ligozzi, C. Bernini, M. G. Bonora, M. De Fatima, J. Zuliani and R. Fontana, *J. Clin. Microbiol.*, 2002, **40**, 1681–1686.
5 K. C. Carroll, B. D. Glanz, A. P. Borek, C. Burger, H. S. Bhally, S. Henciak and D. Flayhart, *J. Clin. Microbiol.*, 2006, **44**, 3506–3509.
6 C. N. Baker, S. A. Stocker, D. L. Rhoden and C. L. Thornsberry, *J. Clin. Microbiol.*, 1986, **23**, 143–148.
7 B. Lamy, S. Dargère, M. C. Arendrup, J. J. Parienti and P. Tattevin, *Front. Microbiol.*, 2016, **7**, 697.
8 O. Opota, K. Jaton and G. Greub, *Clin. Microbiol. Infect.*, 2015, **21**, 323–331.
9 K. D. Lenz, S. Jakhar, J. W. Chen, A. S. Anderson, D. C. Purcell and M. O. Ishak, *et al.*, *Sci. Rep.*, 2021, **11**, 5287.
10 Y.-L. Fang, *Lab Chip*, 2021, **21**, 113–121.
11 K. Zeng, M. Osaid and W. van der Wijngaart, *Lab Chip*, 2023, **23**, 4334–4342.
12 W. G. Pitt, M. Alizadeh, G. A. Husseini, D. S. McClellan, C. M. Buchanan and C. G. Bledsoe, *et al.*, *Biotechnol. Prog.*, 2016, **32**, 823–839.
13 B. Forsyth, *Biosensors*, 2021, **11**, 288.
14 A. J. Mach and D. Di Carlo, *Biotechnol. Bioeng.*, 2010, **107**, 302–311.
15 H. W. Hou, R. P. Bhattacharyya, D. T. Hung and J. Han, *Lab Chip*, 2015, **15**, 2297–2307.
16 X. Lu, J. J. M. Chow, S. H. Koo, B. Jiang, T. Y. Tan, D. Yang and Y. Ai, *Lab Chip*, 2021, **21**, 2163–2177.
17 S. Narayana Iyengar, T. Kumar, G. Mårtensson and A. Russom, *Electrophoresis*, 2021, **42**, 2538–2551.
18 S. Park, Y. Zhang, T. H. Wang and S. Yang, *Lab Chip*, 2011, **11**, 2893–2900.
19 P. Dow, K. Kotz, S. Gruszka, J. Holder and J. Fiering, *Lab Chip*, 2018, **18**, 923–932.
20 P. Ohlsson, K. Petersson, P. Augustsson and T. Laurell, *Sci. Rep.*, 2018, **8**, 9156.
21 J. H. Kang, M. Super, C. W. Yung, R. M. Cooper, K. Domansky and A. R. Graveline, *et al.*, *Nat. Med.*, 2014, **20**, 1211–1216.
22 T. H. Kim, J. Kang, H. Jang, H. Joo, G. Y. Lee and H. Kim, *et al.*, *Nature*, 2024, **632**, 893–902.
23 X. B. Zhang, Z. Q. Wu, K. Wang, J. Zhu, J. J. Xu, X. H. Xia and H. Y. Chen, *Anal. Chem.*, 2012, **84**, 3780–3786.
24 H. Shirinkami, G. Wang, J. Park, J. Ahn, Y. Choi and H. Chun, *Sens. Actuators, B*, 2020, **307**, 127412.
25 P. E. Guevara-Pantoja, *Lab Chip*, 2025, **25**, 4886–4897.
26 T. Zhang, D. Di Carlo, C. T. Lim, T. Zhou, G. Tian and T. Tang, *et al.*, *Biotechnol. Adv.*, 2024, **71**, 108317.
27 I. K. Dimov, *Lab Chip*, 2011, **11**, 845–850.
28 E.-C. Yeh, *Sci. Adv.*, 2017, **3**, e1501645.
29 M. A. Faridi, H. Ramachandraiah, I. Banerjee, S. Ardabili, S. Zelenin and A. Russom, *J. Nanobiotechnol.*, 2017, **15**, 3.
30 A. Burklund and J. X. Zhang, *Ann. Biomed. Eng.*, 2019, **47**, 1657–1674.
31 J. M. Martel, K. C. Smith, M. Dlamini, K. Pletcher, J. Yang and M. Karabacak, *et al.*, *Sci. Rep.*, 2015, **5**, 11300.
32 D. Huh, J. H. Bahng, Y. Ling, H. H. Wei, O. D. Kripfgans and J. B. Fowlkes, *et al.*, *Anal. Chem.*, 2007, **79**, 1369–1376.

33 A. Y. Fu, C. Spence, A. Scherer, F. H. Arnold and S. R. Quake, *Nat. Biotechnol.*, 1999, **17**, 1109–1111.
34 R. M. Cooper, D. C. Leslie, K. Domansky, A. Jain, C. Yung and M. Cho, *et al.*, *Lab Chip*, 2014, **14**, 182–188.
35 S. Hwang and J. Choi, *Lab Chip*, 2023, **23**, 229–238.
36 J. Choi, H. Y. Jeong, G. Y. Lee, S. Han, S. Han and B. Jin, *et al.*, *Sci. Rep.*, 2017, **7**, 1148.
37 P. E. Guevara-Pantoja, Y. Alvarez-Braña, J. Mercader-Ruiz, F. Benito-Lopez and L. Basabe-Desmonts, *Lab Chip*, 2025, **25**, 4886–4897.
38 R. F. Probstein, *Physicochemical Hydrodynamics: An Introduction*, John Wiley & Sons, Hoboken, 2005.
39 T. D. Anyaduba and J. Rodriguez-Manzano, *Micromachines*, 2024, **15**, 1063.
40 D. M. Eckmann, *Anesth. Analg.*, 2000, **91**, 539–549.
41 M. Ghoreishi, E. Senturk, G. Cidonio, C. Scognamiglio, Z. Salajková, M. Riminucci, A. Corsi, G. Ruocco, M. Leonetti and R. Reale, *Microfluid. Nanofluid.*, 2025, **29**, 28.
42 T. M. O'Connell, D. King, C. K. Dixit, B. O'Connor, D. Walls and J. Ducrée, *Lab Chip*, 2014, **14**, 3629–3639.
43 A. Bondesan, L. Girolami, F. James and L. Rousseau, *Phys. Fluids*, 2025, **37**, 043327.
44 M. H. M. Miguélez, M. Osaid, J. Larsson, V. Kandavalli, J. Elf and W. van der Wijngaart, *bioRxiv*, 2024, preprint, DOI: 10.1101/2024.05.23.595289.
45 A. Hijikata-Okunomiya and N. Kataoka, *J. Thromb. Haemostasis*, 2003, **1**, 2060–2061.
46 P. K. Shin, P. Pawar, K. Konstantopoulos and J. M. Ross, *Am. J. Physiol.*, 2005, **289**, C727–C734.